

# Linking Persistent Scatterers to the Built Environment using Ray-Tracing on Urban Models

Mengshi Yang<sup>1,2</sup>, Paco López-Dekker<sup>1</sup>, Prabu Dheenathayalan<sup>1</sup>, Filip Biljecki<sup>3</sup>, Mingsheng Liao<sup>2,\*</sup>, Ramon F. Hanssen<sup>1</sup>

<sup>1</sup> Department of Geoscience and Remote Sensing, Delft University of Technology, 2628 Delft, The Netherlands

<sup>2</sup> State Key Laboratory of Information Engineering in Surveying, Mapping and Remote Sensing, Wuhan University, Wuhan 430079, China

<sup>3</sup> Department of Architecture, National University of Singapore, 4 Architecture Dr, Singapore 117566, Singapore

---

## ORCID

MY: <https://orcid.org/0000-0003-1449-3494>

PLD: <https://orcid.org/0000-0002-0221-4403>

PD: <https://orcid.org/0000-0003-3477-8390>

FB: <https://orcid.org/0000-0002-6229-7749>ML: <https://orcid.org/0000-0001-9556-4287>RFH: <https://orcid.org/0000-0002-6067-7561>

\* Corresponding author at [liao@whu.edu.cn](mailto:liao@whu.edu.cn)

This is an Accepted Manuscript of an article published by IEEE in the journal *IEEE Transactions on Geoscience and Remote Sensing* in 2019, available online:

<http://doi.org/10.1109/TGRS.2019.2901904>

## Cite as:

Yang M, López-Dekker P, Dheenathayalan P, Biljecki F, Liao M, Hanssen RF (2019): Linking Persistent Scatterers to the Built Environment using Ray-Tracing on Urban Models. *IEEE Transactions on Geoscience and Remote Sensing*, 57(8): 5764–5776.

© 2019 IEEE. Personal use of this material is permitted. Permission from IEEE must be obtained for all other uses, in any current or future media, including reprinting/republishing this material for advertising or promotional purposes, creating new collective works, for resale or redistribution to servers or lists, or reuse of any copyrighted component of this work in other works.

## Abstract

Persistent Scatterers (PS) are coherent measurement points obtained from time series of satellite radar images, which are used to detect and estimate millimeter-scale displacements of the terrain or man-made structures. However, associating these measurement points with specific physical objects is not straightforward, which hampers the exploitation of the full potential of the data. We have investigated the potential for predicting the occurrence and location of persistent scatterers using generic 3D city models and ray tracing methods, and proposed a methodology to match PSs to the point-like scatterers predicted using RaySAR, a ray-tracing SAR simulator. We also investigate the impact of the *level-of-detail* (LOD) of the city models. For our test area in Rotterdam, We find that 10% and 37% of the PSs detected in a stack of TerraSAR-X data can be matched with point-scatterers identified by ray-tracing using LOD1 and LOD2 models, respectively. In the LOD1 case, most matched scatterers are at street-level, while LOD2 allows the identification of many scatterers on the buildings. Over half of the identified scatterers correspond to easy to identify double or triple bounce-scatterers. However, a significant fraction corresponds to higher bounce levels, with approximately 25% being fivefold-bounce scatterers.

*Keywords:* synthetic aperture radar (SAR); persistent scatterers; level of detail (LOD); ray tracing; simulation

## 1 Introduction

Persistent Scatterer Interferometry (PSI) [1] is a geodetic technique to measure surface displacements using multi-epoch Synthetic Aperture Radar (SAR) images. PSI estimates the displacement parameters from phase observations from selected coherent points, known as Persistent Scatterers (PS), with millimeter-level precision. Using advanced high-resolution SAR satellite systems, such as TerraSAR-X and COSMO-SkyMed, this technology can be used to monitor individual structures [2, 3, 4, 5, 6].

However, persistent scatterers differ from traditional well-defined geodetic benchmarks. It is not clear whether the observed signal stems from one dominant reflector, like a corner reflector, or from the effective summation of several reflectors within the resolution cell. Moreover, even if the PS is one dominant reflector, its precise localization remains a challenging task. Obviously, the capability to link persistent scatterers to (locations on) particular objects would enhance PSI analyses, for example by reducing the uncertainty in the interpretation of the observed displacements in relation to specific driving mechanisms.

The relevance of establishing a one-to-one link between PSs and specific objects is most obvious when there are different driving mechanisms involved. For example, points may represent deep and/or shallow deformation, e.g. due to gas production and groundwater level changes, respectively. Consequently, nearby PSs may show different deformation signals. In other cases different parts of a building or infrastructure may deform differently, which may be a precursor of a partial or full collapse of the structure. In these complex scenarios, linking persistent scatterers to

the objects in the built environment would not only help identifying the local deformation in the object, but also facilitate the interpretation of the deformation signals.

Using the precise geolocalization of each PS seems to be the most straightforward approach to link the scatterer to an object. In fact, the geolocalization accuracy of PS for high-res (meter-resolution) SAR data is shown to be in the order of centimeters in azimuth and range[7], and several dm up to 1.8 m for cross-range [8]. This positioning uncertainty can be described with a variance-covariance matrix and visualized with an error ellipsoid [9, 10]. This way, the relatively poor cross-range precision of radar scatterers could be improved by intersecting the scaled error ellipsoid with 3D models[9, 10]. Alternatively, an improvement of positioning precision could be obtained by using SAR data from different viewing geometries [11, 12], albeit only for a selected number of targets, such as lamp posts.

Yet, these methods all consider only the *geometry* of the problem, and are not based on physical scattering mechanisms. Consequently, the estimated positions may be geometrically optimal, but physically unrealistic. For example, for a perfect corner reflector, it is known that the effective scattering center is at the apex of the reflector, even though the pure geometric position estimate may turn out to be at a different position. As a result, understanding the *physical* scattering mechanisms may help in the realistic physical positioning of scatterers.

Physical understanding of scattering mechanisms can be supported by SAR simulation methods. However, this requires, at the least, a 3D geometrical representation of the scene (i.e. a 3D city model) [13]. If this 3D representation is realistic with sufficient detail, the observed SAR scene should be very similar to the simulated one. Subsequently, if there is sufficient similarity, we will know which scattering mechanism produced the observed scatterers, and understand what caused the observed displacements.

A list of current SAR simulators includes, but is not limited to, SARAS [14, 15], Pol-SARAS [16], CAS [17], Xpatch 4 [18], GRECOSAR [19], CohRaS [20], SARViz [21], and RaySAR [22]. SARAS and CAS are oriented to ocean applications and do not consider multiple scattering for complex targets [14, 15, 17]. Pol-SARAS is the polarimetric version of SARAS, and it allows the simulation of natural scenes [16]. Xpatch 4 is an object-oriented version of Xpatch, which provides 0-D radar cross section, 1-D range profile, 2-D SAR image, and 3-D scattering center signatures, based on the shooting and bounces rays with supporting of parallel computation [18]. Xpatch has been widely used in studies of the vehicle, typically an airplane or a ground vehicle [23, 24, 25]. GRECOSAR can generate polarimetric SAR (POLsar) and polarimetric inverse SAR (POLisar) images of complex targets, and is used extensively for vessel classification studies [19]. CohRaS is a SAR simulator based on ray tracing, mainly for small scenes with high resolution, and only supports geometries made up of convex polygons [20]. SARViz is a SAR image simulation system which only simulates single and double bounce reflections and does not include coherent addition of multiple echos [21]. Finally, RaySAR is based on ray-tracing, oriented towards the simulation of salient features in SAR images [26, 27, 28]. Despite the natural limitations resulting from the ray-tracing approach, it has some key advantages that motivated its use for the research presented in this study: (i) it can handle an arbitrary number of bounces, (ii) it keeps track of individual scatterers, (iii) providing their 3D location and bounce level; and (iv) it is computationally inexpensive, which allows the simulation of relatively large and complex urban scenes.

Here we investigate the potential for predicting the occurrence and location of SAR scatterers (i.e. potential PS) based on physical scattering mechanisms, using generic 3D city models. In particular, we analyze the influence of the *level of detail* (LOD) of these city models on this prediction. The LOD is a generic metric describing the degree of adherence of the dataset to its real-world counterpart [29]. The paper focuses on the urban environment, where we are limited by the short supply of high resolution 3D city models. We use the ray-tracing SAR simulator RaySAR [22] to predict the radar scattering by illuminating the 3D scene with a SAR sensor. The *rays* can follow multiple reflections within the object scene, yielding a collection of point-like multiple-bounce scatterers that represent potential PS candidates. The use of ray-tracing algorithm implies that a significant part of the radar signal is not correctly modeled. Nevertheless, city models with a level of detail that allows a full electromagnetic solution are not available nor expected to become available in the foreseeable future.

Section 2 introduces the 3D ray-tracing simulation as well as the methodology to match the detected PSs with the Simulated Point-Scatterers (SPS). Results corresponding to a test-area in Rotterdam are presented and analyzed in Section 2.3. Finally, Section 4 presents our conclusions and future work.

## 2 Methodology

### 2.1 Point Scatterer Simulation with RaySAR

Ray tracing is a rendering method used to create an image by following the path of a ray through a 3D model and simulating the reflections on the surfaces it encounters. Ray tracing is based on geometrical optics, which is valid for surfaces that are large and smooth relative to the wavelength. RaySAR is one of the several SAR data simulators based on ray tracing. It is built on the open source Persistence of Vision Ray-tracer (POV-Ray) [30], using the PoV-Ray basic algorithms for ray tracing, intersections tests between rays and objects, the estimation of intensities, shadow calculations, etc [22].

RaySAR generates a set of scattering centers positioned in 3D SAR coordinates, i.e., azimuth, range, and cross-range. RaySAR subsequently projects and interpolates these scatterers on the 2D range-azimuth grid, adding the different contributions coherently in order to generate a simulated SAR image. In this study, however, we are mostly interested in the intermediate set of individual scatterers.

The set of scattering centers is provided by RaySAR as a list of signal vectors  $V$ :

$$V = [a_i \ r_i \ c_i \ I \ b \ f] \quad (1)$$

where  $[a_i \ r_i \ c_i]$  gives the position of the scattering phase center in azimuth, range, and cross-range,  $I$  is a relative intensity normalized between 0 to 1,  $b$  specifies the number of bounces (trace level), and  $f$  is a boolean indicating a specular reflection [0 or 1]. The signals  $V$  are referred to

as contribution signals. These signals are the basis for the simulated image generation and point scatterers identification.

Fig. 1 sketches the localization of the phase-center of a radar echo by RaySAR for a double bounce signal. Starting from the virtual sensor plane, a primary ray for each pixel is followed along its path until intersection with the modeled scene is found. At the intersection point, a reflected ray is spawned in the specular direction, and traced until the next intersection with the model, and so on. The azimuth, cross-range and range coordinates of the double-bounce signal are given by

$$\begin{aligned} a_i &= \frac{a_1 + a_2}{2} \\ c_i &= \frac{c_1 + c_2}{2} \\ r_i &= \frac{r_1 + r_2 + r_3}{2}. \end{aligned} \quad (2)$$

The trace level is the number of bounces of the signal.

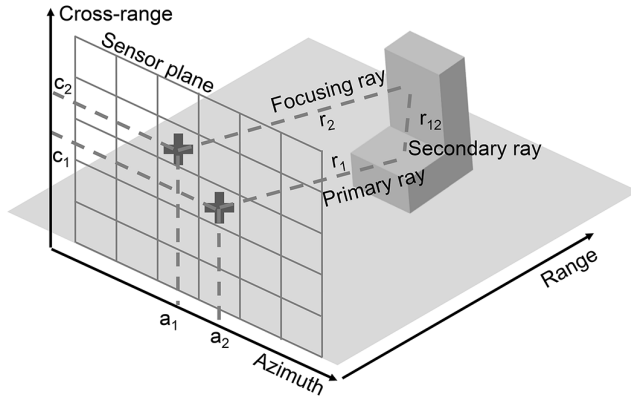


Figure 1: Sketch of how RaySAR localizes a double bounce signal and projects it in the sensor plane.

To select potential PS candidates (simulated Point-Scatterers), contribution signals with specular multiple scattering characteristics ( $I > 0$ ,  $b > 1$ , and  $f = 1$ ) are chosen. The selection criteria are based on the premise that many PSs are physically associated with multiple specular reflections of the radar signal on relatively large surfaces.

## 2.2 Definition of a 3D Scene for RaySAR

The input to RaySAR is a 3D scene model including (i) a virtual SAR system, (ii) 3D building models, (iii) surface parameters.

### 2.2.1 Virtual SAR system

The virtual SAR system is described by the observation geometry and the system resolution. The geometry is defined using an orthographic projection and a parallel ray approximation. This parallel ray approximation makes the observation geometry azimuth invariant, as it should. However, it also makes the geometry elevation (hence range) invariant, which is not entirely correct. We will, nevertheless, assume that this approximation is good enough for a small scene. Thus, the observation geometry is defined by an incident angle and an azimuth angle with respect to the scene, which has to be specified in RaySAR as a position of the sensor with respect to the center of the scene.

### 2.2.2 3D scene model

In this research, the building model is reconstructed with 3dfier [31] by combining the large-scale topographic dataset of the Netherlands, BGT ('*Basisregistratie Grootchalige Topografie*' in Dutch) dataset and the laser altimetry, AHN3 ('*Actueel Hoogtebestand Nederland*' in Dutch) datasets. The acquisition of 3D models can be constructed directly with a text editor or software which can assist in visual controlling modeling (e.g., CAD). Importing available 3D model into the POV-Ray format is an option considering there are a lot of city models available.

The 3D object model has to provide sufficient geometric detail for SAR simulation. The amount of detail and spatial resolution of a 3D city model are specified as LOD, denoting the abstraction level of a model as opposed to the real world object [29]. The LODs have been described by CityGML [32], a prominent standard for the storage and exchange of 3D city models. LOD1 is a model in which buildings are represented as blocks (usually obtained by extruding their footprint to a uniform height). LOD2 is a more detailed model including roof shapes [32, 33]. As it is the case with many other applications of 3D city models [34], it is to be expected that the LOD and quality of the used 3D model will have an influence on the performance of the simulation of radar signals, a topic which we investigate in this paper.

### 2.2.3 Surface Parameters

The scattering properties of the scattering surfaces in the 3D model are specified by the parameters described in Table 1. The first parameter,  $F_w$ , controls multiple scattering by setting the fraction of the ray intensity that is specularly reflected. Thus, setting  $F_w = 0$  will completely suppress multiple scattering.

The second parameter,  $F_s$ , controls the relative intensity of the first reflection, counting from the illumination source. The roughness parameter,  $F_r$ , controls the angular width of the first reflection. Values of low roughness and medium roughness surfaces are given based on a constant relative permittivity of  $5.7 + j \cdot 1.3$  for man-made objects [22].

Fig. 2 shows 4 images simulated with varying  $(F_w, F_s, F_r)$  values according to the Table 1. The parameter  $F_r$  works with specular coefficient  $F_s$ , see Fig. 2a and 2b. With increasing roughness,

Table 1: Surface Parameters

Parameters		Impact on Radar Scattering	Value range	Low Roughness	Medium Roughness
Weight	$F_w$	Weights the specularly reflected signal on a surface (loss of signal strength) of multiple reflections and works with a specular coefficient.	0 - 1	0.7	0.5
Specular	$F_s$	Resembles specular reflection and provides a spreading of the highlights occurring near the object horizons.	0 - 1	0.7	0.5
Roughness	$F_r$	Defines the width of a cone where a specular highlight occurs from 1 (very rough) to 0 (very smooth).	0 - 1	$8.5 \cdot 10^{-4}$	$3.3 \cdot 10^{-3}$

the number of features seen in the simulated images increases. Fig. 2c and 2d illustrate the results of a combination of three parameters. With the weight factor  $F_w$ , the strong multi-scattering is clearly described. The intensity of a multi-reflected signal is weighted with the  $F_w$ . In this research, we use the medium roughness  $F_w = 0.5, F_s = 0.5, F_r = 3.3 \cdot 10^{-3}$ , comparing to low roughness parameter setting, medium roughness parameters are closer to the reality using the X-band data, see Fig. 2e. It is important to emphasize that the phase-center location of the simulated scatterers does not depend on the surface parameters. Below, we focus solely on the phase-center location of multiple-bounce SPSs.

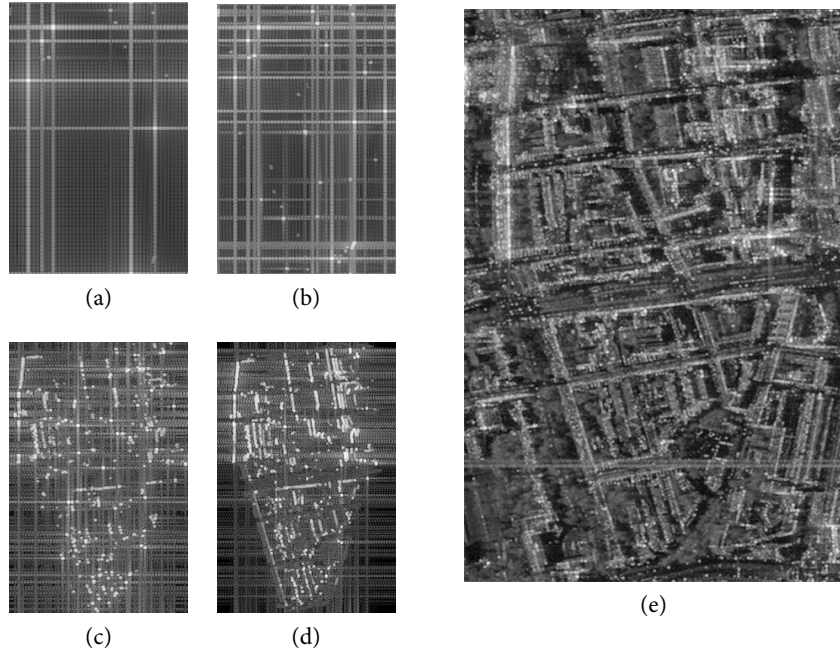


Figure 2: Parameters function on SAR image simulation, (a) image with  $F_w = 0, F_s = 0.7, F_r = 8.5 \cdot 10^{-4}$ , (b) image with  $F_w = 0, F_s = 0.5, F_r = 3.3 \cdot 10^{-3}$ , (c) image with  $F_w = 0.7, F_s = 0.7, F_r = 8.5 \cdot 10^{-4}$ , (d) image with  $F_w = 0.5, F_s = 0.5, F_r = 3.3 \cdot 10^{-3}$ , (e) Mean intensity map of 49 TerraSAR-X images.

### 2.3 Linking of Simulation Points with PSs

One of the main steps in the work presented is the matching of the SPSs with the PSs identified in the InSAR time series. The matching is done by evaluating the weighted Euclidean distances between the positions of the simulated point-scatterers and the positions of the PSs. The weighting reflects the 3D position error ellipsoids, as defined by the positioning Variance-Covariance (VC) matrices, of the PSs [9]. For each PS, the positioning uncertainty in the local reference frame (East, North, and Up/Height) is given by

$$\mathbf{Q}_{enh} = \mathbf{R}_{3 \times 3} \cdot \mathbf{Q}_{rac} \cdot \mathbf{R}_{3 \times 3}^T = \begin{bmatrix} \sigma_e^2 & \sigma_{en}^2 & \sigma_{eh}^2 \\ \sigma_{en}^2 & \sigma_n^2 & \sigma_{nh}^2 \\ \sigma_{eh}^2 & \sigma_{nh}^2 & \sigma_h^2 \end{bmatrix} \quad (3)$$

where  $\mathbf{R}$  is the rotation matrix from radar geometry to local reference frame,  $\mathbf{Q}_{rac}$  the positioning VC matrix in 3D radar geometry with diagonal component variances ( $\sigma_r^2, \sigma_a^2, \sigma_c^2$ ) in range, azimuth and cross range, the diagonal ( $\sigma_e^2, \sigma_n^2, \sigma_h^2$ ) and non-diagonal ( $\sigma_{en}^2, \sigma_{eh}^2, \sigma_{nh}^2$ ) are the variances and covariances in east, north and up coordinates. For each PS, from the eigenvalues of  $\mathbf{Q}_{enh}$ , a 3D error ellipsoid is drawn with the estimated position as its center. The semi-axis lengths of the ellipsoid are described by the eigenvalues of  $\mathbf{Q}_{enh}$ , which are  $\sigma_r^2, \sigma_a^2, \sigma_c^2$ . The shape of ellipsoid is derived from the ratio of their axis lengths, given by  $(1/\gamma_1 / \gamma_2)$ , where  $\gamma_1 = \sigma_a \cdot \sigma_r^{-1}$ , and  $\gamma_2 = \sigma_a \cdot \sigma_r^{-1}$ . The orientation of ellipsoid is dependent on the local incidence angle of the radar beam at the PSs.

Fig. 3 illustrates the matching of an SPS with a PS based on the 3D error ellipsoid. The position uncertainty of a PS is illustrated by 3D error ellipsoid with 0.01 level of significance. The PS is matched to the corresponding SPS, which has to be inside the error ellipsoid.

As part of the matching process, it is necessary to consider and remove potential systematic positioning errors. The systematic errors may be the result of an oversimplified geometry (e.g. the already mentioned range invariance), or errors in the knowledge of the acquisition SAR geometry.

A fine coregistration is performed using the Iterative Closest Point (ICP) algorithm [35, 36], which minimizes the sum of the weighted Euclidean distance between SPSs and PSs by Least Square Estimation (LSE) in an iterative way. Each iteration of the 3D error ellipsoid based ICP includes two steps: matching pairs of SPS and PSs based on the 3D error ellipsoid; and finding the transformation that minimizes the weighted mean squares distance between pairs of points. The transformation results are applied to the point cloud of PSs, thereby changing the correspondence.

### 2.4 Simulation Assessment

A quantitative evaluation of the matching between the PS and the Simulated Point Scatterer (SPS) is given by the confusion matrix  $\mathbf{M}$  described in Table 2. Three performance ratios are considered:

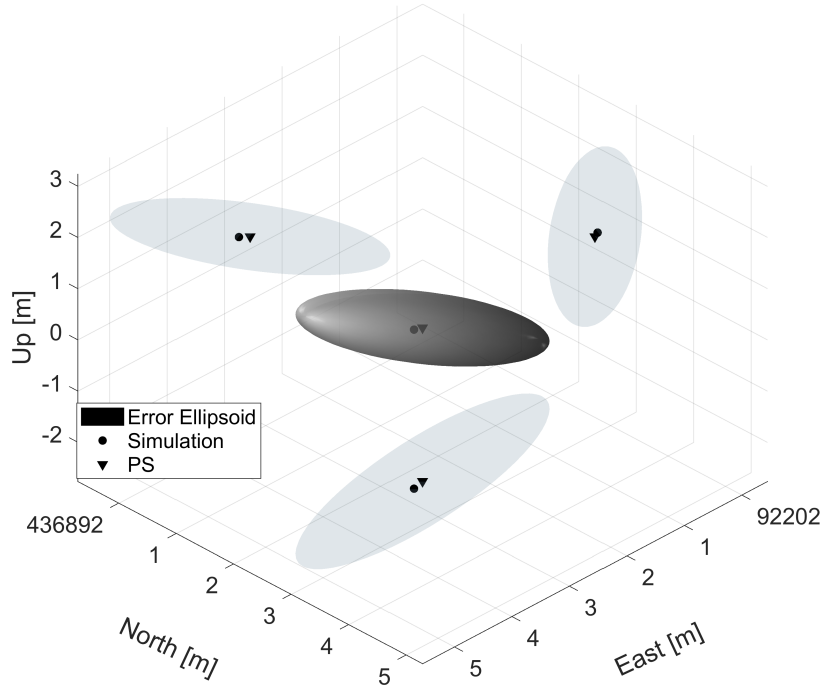


Figure 3: An example of finding the corresponding simulation point of a PS based on the 3D error ellipsoid. The position of the PS is indicated by a black triangle. A cigar-shaped error ellipsoid with a ratio of axis lengths 1/2/35 (with  $\sigma_r = 0.019$  m) illustrates the PS position uncertainty. The corresponding SPS is located inside of the error ellipsoid and indicated by a black dot. The ellipsoid and PS are projected in east-north, north-up, and up-east planes to illustrate their intersection with the SPS.

- **True Positive Rate (TPR):** the ratio of the PSs that are matched to SPSs, with regards to the total number of PSs.
- **False Negative Rate (FNR):** the ratio of the PSs that have not been matched to an SPS, with regards to the total number of PSs, also known as miss rate. For FNR, we have  $FNR = 1 - TPR$ .
- **False Positive Rate (FPR):** the ratio of the SPSs that have not been matched, with regards to the total number of SPSs.

Hereby, the metric TPR describes the matching ratio between simulation points and PSs, and is the primary evaluation indicator of simulation scatterers. FPR also an important indicator for describing the ratio of redundant simulation points.

Table 2: Confusion matrix  $\mathbf{M}$  between SPS and PS

		SPSs	
		Match	Non-Match
PSs	Match	True Positive Rate(TPR) $= \frac{\sum TP}{\sum PSs}$	False Positive Rate(FPR) $= \frac{\sum FP}{\sum SPSs}$
	Non-Match	False Negative Rate(FNR) $= \frac{\sum FN}{\sum PSs}$	

Note that the PS or SPS selection criteria will have an impact on the performance metrics. For example, a low amplitude dispersion threshold may lead to selecting less actual point-scatterers and lead to a higher FPR. Since the final goal of our research is to improve our capability to analyze deformation signals, we focus on the group of PSs that are deemed reliable. PSs are chosen with an amplitude dispersion threshold set to 0.45 and further checked based on network phase consistency [37]. Here, SPSs are scatterers predicted by the simulator based on the geometry. Therefore, the final number of PSs is less than the SPSs from the simulator, because we eliminated many points during the PSI processing, which increases the FPR.

## 2.5 Work-flow

The flowchart in Fig 4 outlines the work-flow of this research, which consists basically of three parts: generation of simulation points, detection of PSs, and the matching of two point cloud sets. The generation of simulation points consists of scene modeling, signals detection with Pov-Ray, and selection of PSPs. The SAR data-stack is processed with the Delft implementation of Persistent Scatterer Interferometry(DePSI) [37], which is based on the Delft framework of geodetic estimation, testing, and quality control. DePSI detects PS with consistent reflection properties over time as input for time series deformation and height estimation. Then, matching of two point cloud sets is carried by ICP based on the 3D error ellipsoid.

RaySAR is not demanding in terms of computational resources. It is built on POV-ray, an open source tool which traces rays in reverse direction. In this study, the calculation of 48 million contribution signals took about 10 minutes on a 4-core workstation with 16 GB of RAM.

## 3 Experiment

### 3.1 Test Site and Data

The test area is located southeast of Rotterdam Central Station in the city of Rotterdam, the Netherlands. The size of the area of interest (AoI) is around  $1 \times 0.5 \text{ km}^2$ . Fig. 5 shows an overview of the test site, and its orientation with respect to the trajectory of TerraSAR-X. 49 TerraSAR-X

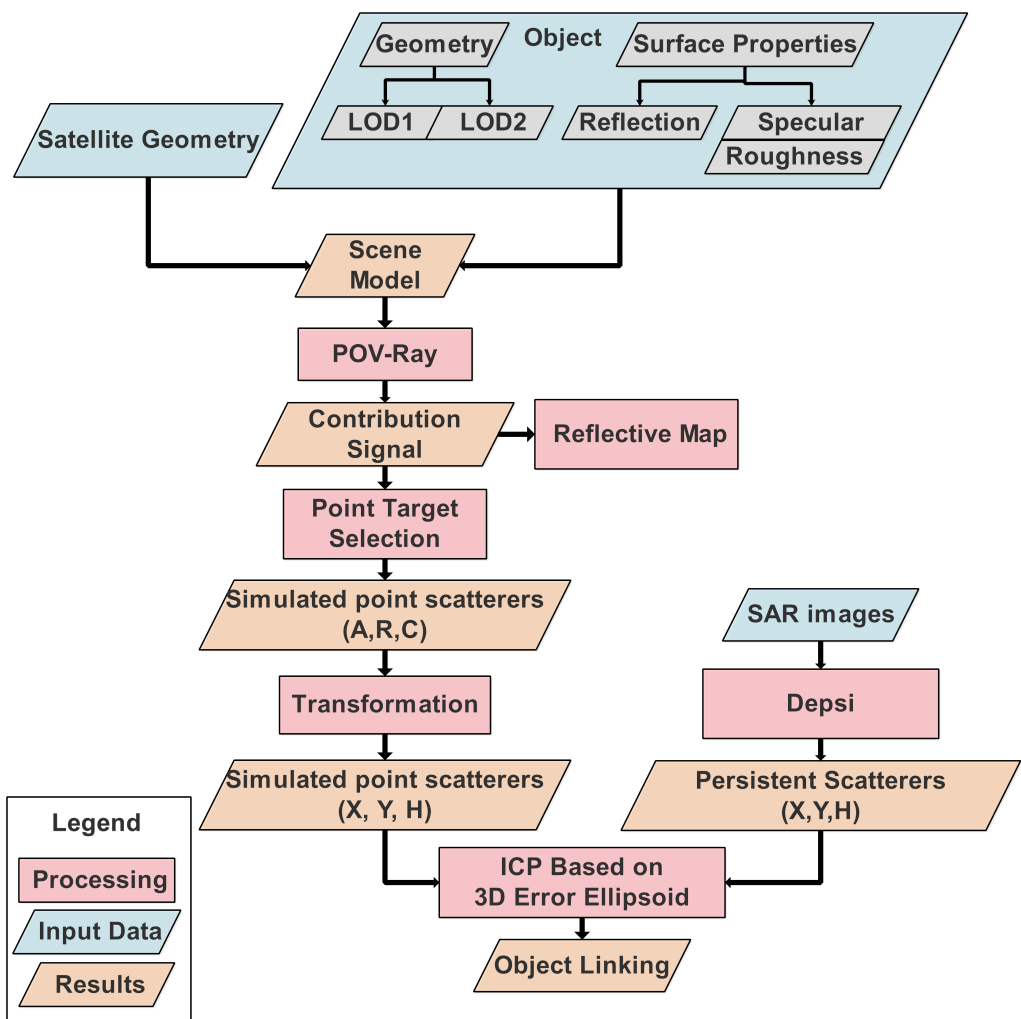


Figure 4: Schematic of the methodology.

strip-mode images are obtained from 19-Jan-2014 to 25-Feb-2017. Table 3 gives the basic parameters of TerraSAR-X data. Fig. 2e is the mean intensity map of 49 TerraSAR-X images over the AOI.

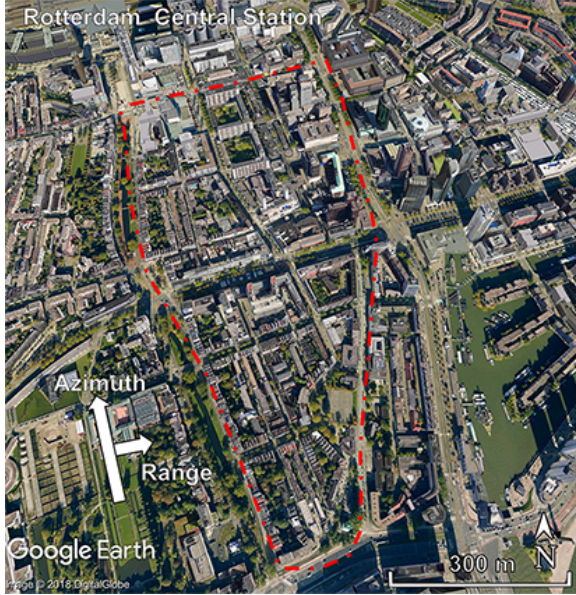


Figure 5: Google Earth overview image of test site, Azimuth and range direction indicate the view of TerraSAR-X data.

Fig. 6 shows a polar histogram describing the orientation of the streets within the AOI calculated based on OpenStreetMap [38]. The direction of each bar represents the compass bearings of the streets and its length indicates the relative frequency of streets with those bearings. From Fig. 6, two main orthogonal directions can be identified, one at about  $336^\circ$  (red bars), and another at about  $60^\circ$  (cyan).

The results of the PSI analysis are illustrated in Fig. 7: 2290 points are selected as PS in the AoI. The results are projected in the Dutch National Reference system RD ('*Rijksdriehoeksstelsel*' in Dutch) and vertical NAP ('*Normaal Amsterdams Peil*' in Dutch) reference system. The axes of Fig. 7 show X (RD) and Y (RD) in meters, in East and North direction, respectively. The estimated heights are indicated by colors, showing some higher buildings in the northwest and northeast corner of the AoI, which can be found in Fig. 5.

Two 3D city models with different level of detail (LOD) were employed to simulate scatterers using RaySAR. Fig. 8 displays the 3D models at LOD1 and LOD2 of the AoI. In LOD1 model, buildings are represented as boxes with flat roof structures (Fig. 8b), opposed to buildings in LOD2 (Fig. 8c), which have differentiated roof structures with varying heights, providing a more realistic representation of the reality.

From the enlarged partial picture of the LOD1 model (Fig. 8b) and the LOD2 model (Fig. 8c), it is clear that buildings in LOD2 include many different parts with varying roof shapes and heights.

Table 3: Basic parameters of TerraSAR-X data stack

Satellite/Parameter	TerraSAR-X
Track	T025
Band(wavelength in cm)	X (3.1)
Start Date	2014.01.19
End Date	2017.02.14
Number of images	49
Acquisition mode	SM
Pass direction	Ascending
Polarization	HH
Pulse Repetition Frequency(Hz)	3790
Range Sampling Rate (MHz)	109.8
Incident angle (°)	39.3
Heading (°)	349.8
Slant range spacing (m)	1.36
Azimuth spacing (m)	1.86
Range Bandwidth (MHz)	100
Azimuth Bandwidth (Hz)	2765

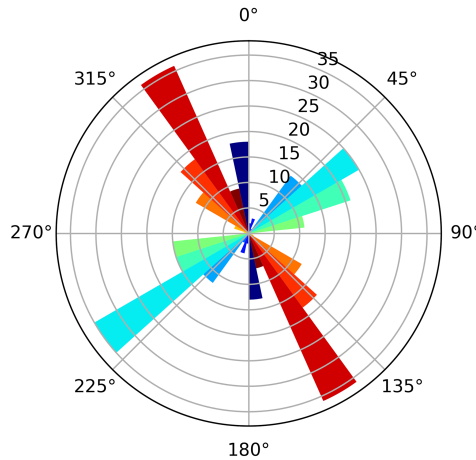


Figure 6: Street orientation map of the AOI. Each bar represents the compass bearing of the streets and its length indicates the frequency of streets with those bearings. There are two main directions at  $336^\circ$  and  $60^\circ$ .

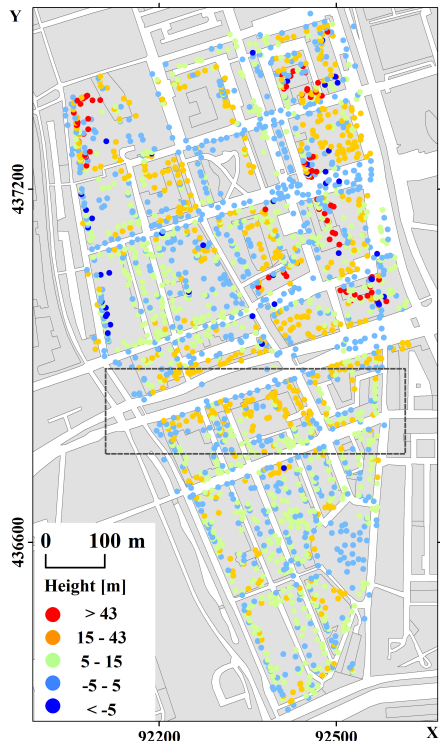


Figure 7: PS identified in TerraSAR-X data stack overlaid on TOP10NL map. TOP10NL is the digital topographic base file of the Land Registry, the most detailed product within the Basic Registration Topography (BRT). The colors indicate the estimated PS heights (blue-low; red-high).

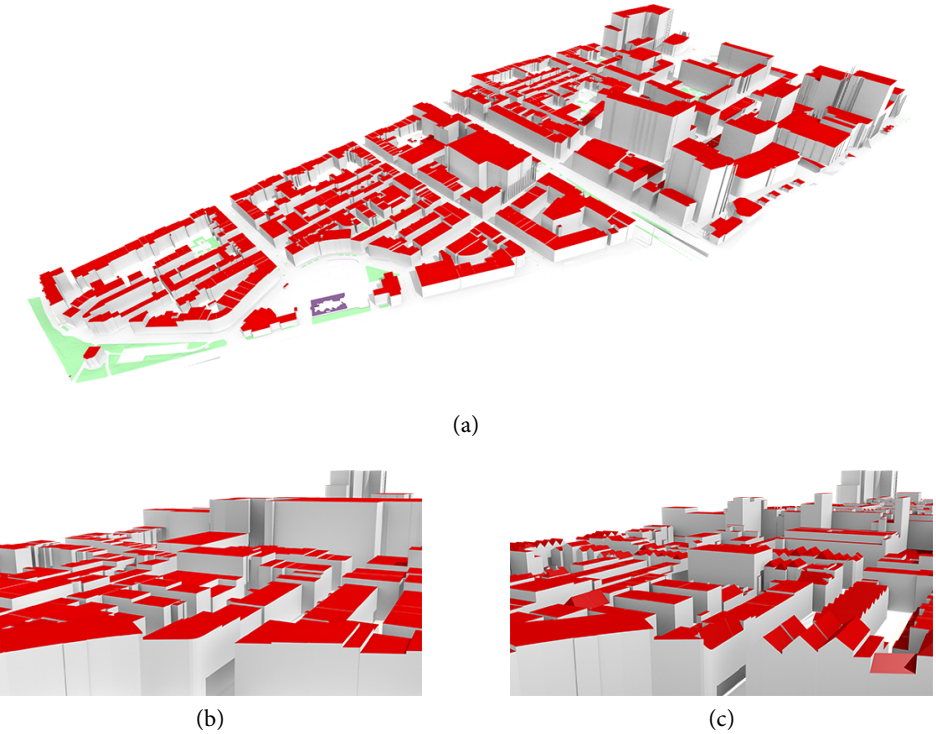


Figure 8: (a) Overview of the used 3D city model; (b) a closer look on the LOD1 variant of the dataset; and (c) its more detailed (LOD2) counterpart including roof shapes. Source of data: BGT, AHN, and City of Rotterdam.

Datasets with LOD1 and LOD2 are the most common instance in practice because it is possible to obtain them automatically, e.g. from LiDAR data by automatic building reconstruction [33].

### 3.2 Simulated Point Scatterer

POV-Ray/RaySAR detects all contributing signals within the AoI. The total number of received signals from the LOD1 and LOD2 models is about 50 million. We detect potential point scatterers, and consider these as signals that exhibit the characteristics of PS ( $I > 0$ ,  $b > 1$ , and  $f = 1$ ) from the contribution signals.

We identify 2770 potential point scatterers from the model at LOD1, as described in Section 2. Fig. 9a shows the distribution of simulated points in the LOD1 model. The colors indicate the height of simulation points. In comparison to the real radar results in Fig. 7, the height values of the SPSs is mainly below 15 m. The simulation points include 742 double bounces, 890 triple bounces, 590 fourfold bounces, and 548 five-fold bounces, see the pie chart in the up-right of the Fig. 9a. Most signals correspond to triple-bounce scatterers, followed by double-bounce ones.

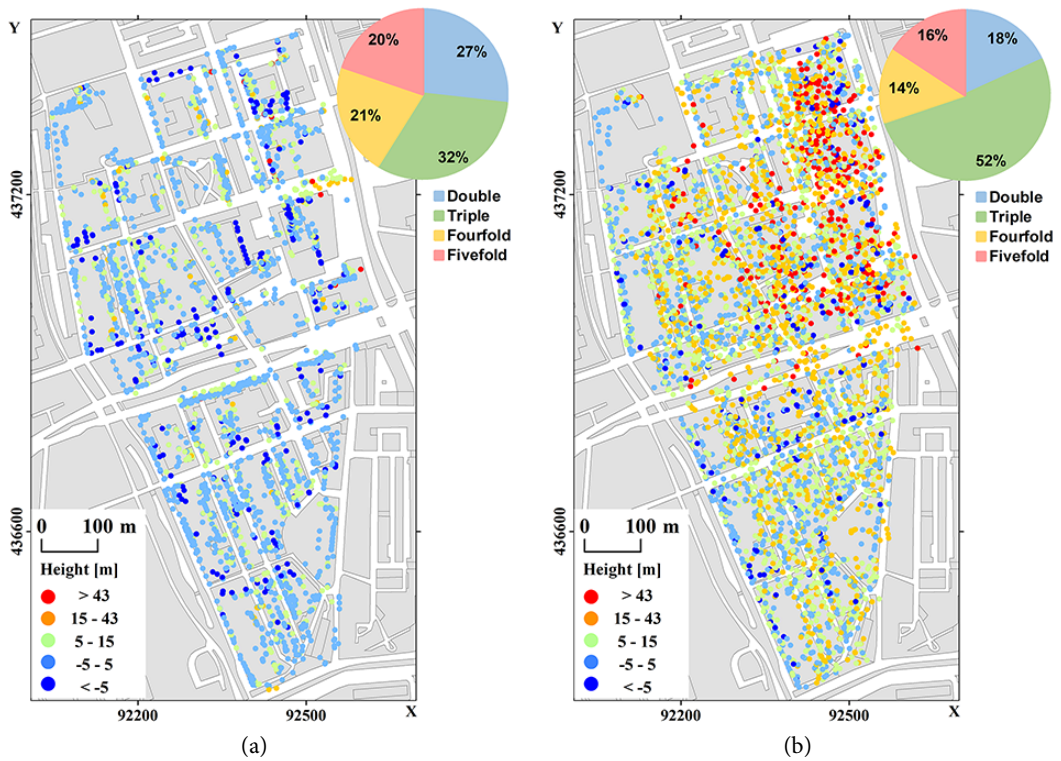


Figure 9: (a) Point scatterers simulated based on model of LOD1 with color represents height, (b) Point scatterers simulated based on model of LOD2 with color represents height. The background image is TOP10NL map.

Using the LOD2 model results in 4390 potential point scatterers, as illustrated see Fig. 9b. Compared to the real PS data, see Fig. 9b, more points, and with higher heights are detected. Spatial distribution in height values of SPSs from the LOD2 model is similar to the measured PS, see Fig. 7. PSs with higher heights are clustered in the northeast corner of the test site, which is also predicted by the simulation. The height of simulation points in the corner of the northwest is lower than PSs in Fig. 7, because the buildings in the corner of the northwest are missed in the LOD2 model(equal to LOD1). The Google Earth image in Fig. 5 also indicate the newly-built in the corner of the northwest. Simulated points from the LOD2 model include 799 double bounce, 2267 triple bounce, 632 fourfold bounce and 692 five-fold bounce, see the pie chart in the up-right of the Fig. 9b. More than half of the points are the triple bounces.

Fig. 10 gives the height profile of PSs, the SPSs of LOD1 and LOD2, in the box indicated in Fig. 7 along the  $x$ -axis. The height profile of PSs and SPSs from LOD2 is similar, while the SPSs from LOD1 missed points with higher height.

### 3.3 Linking of PSs and SPSs

Following Section 2.3, PSs (Fig. 7) were matched to the point-scatterers predicted using the LOD1 (Fig. 9a) and LOD2 (Fig. 9b) models. Fig. 11a and Fig. 11b show the spatial distribution of PSs and the corresponding SPSs. The dark circle indicates the location of PSs that have been matched to SPSs. The dots represent the corresponding SPSs, color-coded by bounce level (see legend on Figure).

Table 4 gives the confusion matrix between SPSs based on LOD1 and LOD2 models and PSs. Scatterers from the model of LOD1 predicted 10% PSs correctly (correspondingly, around 90% PSs were missed). 92% simulation points have not been matched to a PS. By using the LO2 model, the amount of PSs matched with simulated scatterers increased to 37%. Naturally, the number of predicted point-targets not matched to PSs also increased. However, it is noteworthy, that, in relative terms, the number of scatterers matched to PSs grew much stronger than the overall amount of predicted scatterers. Moreover, the ratio of simulation points that have not match to a PS is decreased to 80%.

Table 4: Confusion Matrix between Measured PSs and predicted scatterers based on LOD1 model, and LOD2 model

		SPSs-LOD1 (2770)		SPSs-LOD2 (4390)	
		Match	Non-Match	Match	Non-Match
		223	2547	842	3548
		TPR	FPR	TPR	FPR
PS	10%	92%		37%	80%
(2290)	FNR			FNR	
	90%			63%	

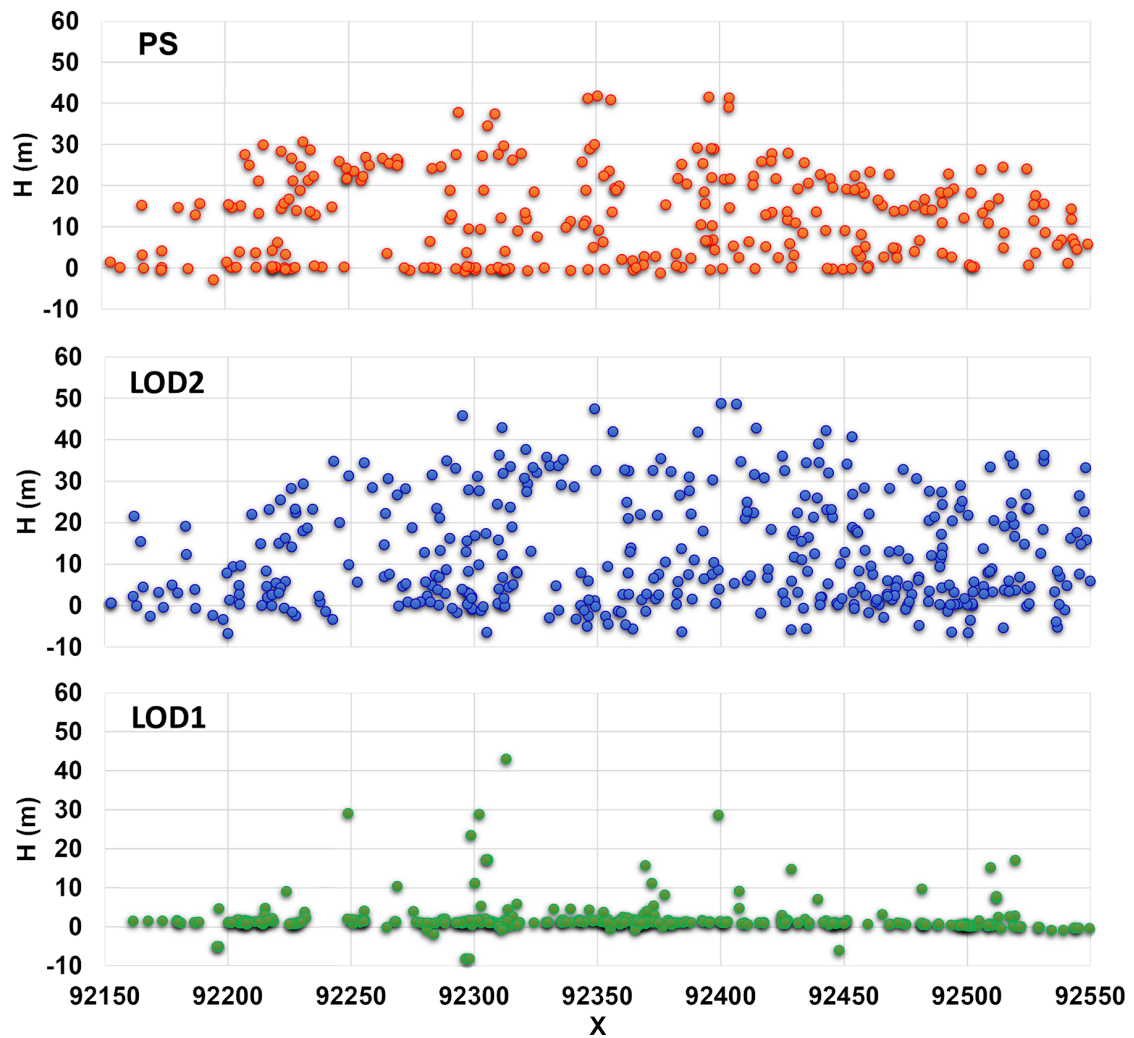


Figure 10: Height profile of PSs, SPSs from LOD1 and LOD2, in the box indicated in Fig. 7 along the  $x$ -axis.

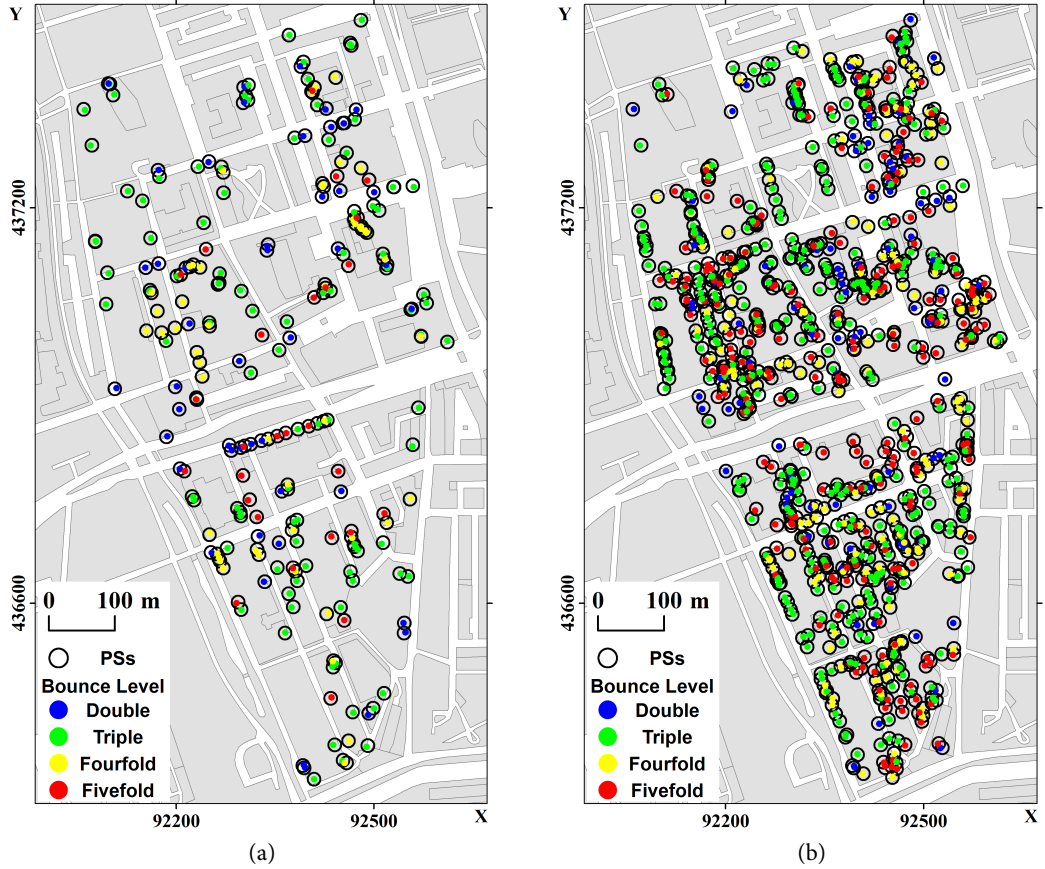


Figure 11: Correspondence between simulated point-scatterers, shown as solid circles color-coded by bounce level, and matched PSs, shown as empty circles. The left panel (a) and the right panel (b) correspond to simulations using the LOD1 and LOD2 models, respectively.

Fig. 12 provides a quantitative overview of the number of point-scatterers predicted for the LOD1 and LOD2 models, segregated by bounce level. In each of the bars, it is also indicated which fraction of the SPSs was matched to a PS. Not surprisingly, the increase of the level of detail leads to a very strong growth (close to a factor 3) of the predicted triple-bounce scatterers. The fraction of predicted triple-bounce scatterers matched to actual PSs increased from 11% to 16%.

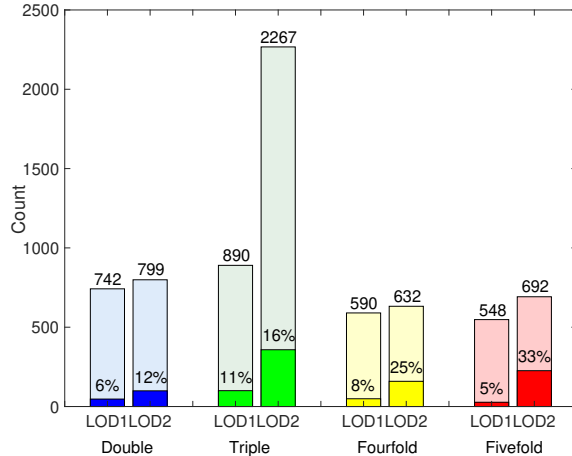


Figure 12: The histograms of simulation points from LOD1 model and LOD2 model in Double, triple, fourfold and fivefold bounce. The X-axis is LOD1 and LOD2. The Y-axis is the count numbers from 0 to 2500. There were 742 and 799 double-bounce signals from LOD1 and LOD2 model. Among these signals, 6% and 12% points were linked to the PSs. Likewise, for triple-bounce signals, and fourfold-bounce signals and fivefold-bounce signals.

For the other bounce-levels considered, the increase of predicted scatterers was quite modest. However, the fraction of these scatterers that was matched to PSs increased by a factor two for double-bounce scatterers, a factor three for fourfold-bounce scatterers, and by more than a factor six for fivefold-bounce scatterers.

The total number of matched scatterers increased from 223 in the LOD1 case, to 842 with the LOD2 model. Triple-bounce scatterers, 100 and 358, respectively, remained dominant. However, 226 of the LOD2-model scatterers, or about one-fourth of the total, corresponded to fivefold-bounce signals.

The number of predicted point-scatterers for the LOD1 (2770) and LOD2 (4390) models were larger than the number of detected PSs. This can be explained by considering that PS selection is done based on the amplitude stability of individual resolution cells in the interferometric data stack. Typically, the amplitude will be stable if a single point-like scatterer is a dominant factor in the radar echo for that resolution cell. Thus even if we know for sure that we have a stable point-like target within our resolution cell, as this does not exclude contributions from other scattering mechanisms, it does not imply that it will result in a PS. Moreover, as stated in section 2.4, the selection criterion also contributes to the fact that the number of simulation points was larger than the number of PSs.

### 3.4 Target matching validation

A potential pitfall in the matching process is that if the local density of either PSs or SPSs is higher, the amount of random matches increases as well (false positives). However, the amount of random matches should be insensitive to their exact position. Hence, while some pairs would be disassociated, roughly the same number is expected to appear.

Following this reasoning, we added random disturbances with Gaussian distribution to the coordinates of the simulated points and performed the PS matching, following the procedure discussed in Section 2. In order to consider the worst case, the random disturbances are aligned along the dominant orientation of the buildings. The  $x$ ,  $y$ , and  $z$  coordinates of the simulated points with random disturbances are given by

$$\begin{aligned}\tilde{x}_{\text{sim}} &= x_{\text{sim}} + \Delta x \\ \tilde{y}_{\text{sim}} &= y_{\text{sim}} + \Delta y \\ \tilde{z}_{\text{sim}} &= z_{\text{sim}} + \Delta z,\end{aligned}\tag{4}$$

where  $x_{\text{sim}}$ ,  $y_{\text{sim}}$ , and  $z_{\text{sim}}$  are the original coordinates of the simulated point scatterers,  $\Delta x = n_1 \cdot \sin(t)$ ,  $\Delta y = n_1 \cdot \cos(t)$ , and  $\Delta z = n_2$ . The angle  $t = 336^\circ$  is the main orientation angle of the streets and buildings as presented in Fig. 6.  $n_1$  and  $n_2$  are zero-mean Gaussian-distributed random disturbances with a standard derivation of  $\sigma$  meter.

Fig. 13 shows the number of matched PSs as a function of  $\sigma$ . The number of matched pairs decreases rapidly as the position disturbance  $\sigma$  increases. Introducing a position error with  $\sigma = 4$  m, which is close to the spatial resolution of TerraSAR-X in stripmap mode, reduces the amount of matches by a factor 4, while a further increase in the positioning error has only a limited effect on decreasing the amount of matches. As less than 10% of the number of matches remains if the positioning error is increased to an unrealistically high value, this analysis suggests that the vast majority of matched pairs are physically correct.

Fig. 14 shows all PSs detected in the area of interest, with identified PSs represented by green triangles and unidentified PSs indicated by magenta plus-signs. The area labeled A, where most PSs were missed by the simulation, correspond to a newly built building not present in the LOD2 model. Moreover, the building model did not include the public facilities, like the flower boxes in the area labeled B. Most predicted PSs are located at linear structures of buildings and identified as triple bounce, such as the points in the area labeled C. Those scatterers originated from the roof and ghost corners e.g. the corner of the wall and the ground, which is in agreement with previous research[28].

Simulation points have precise locations and precise location in the model. The object snap of PSs can be achieved by the correlation of PSs and SPSs. Fig. 15 displays an overview of matched simulation points in LOD2 model. The supplementary file of this research includes a movie that is a 360-degree view of model and simulation points that matched to measured PSs.

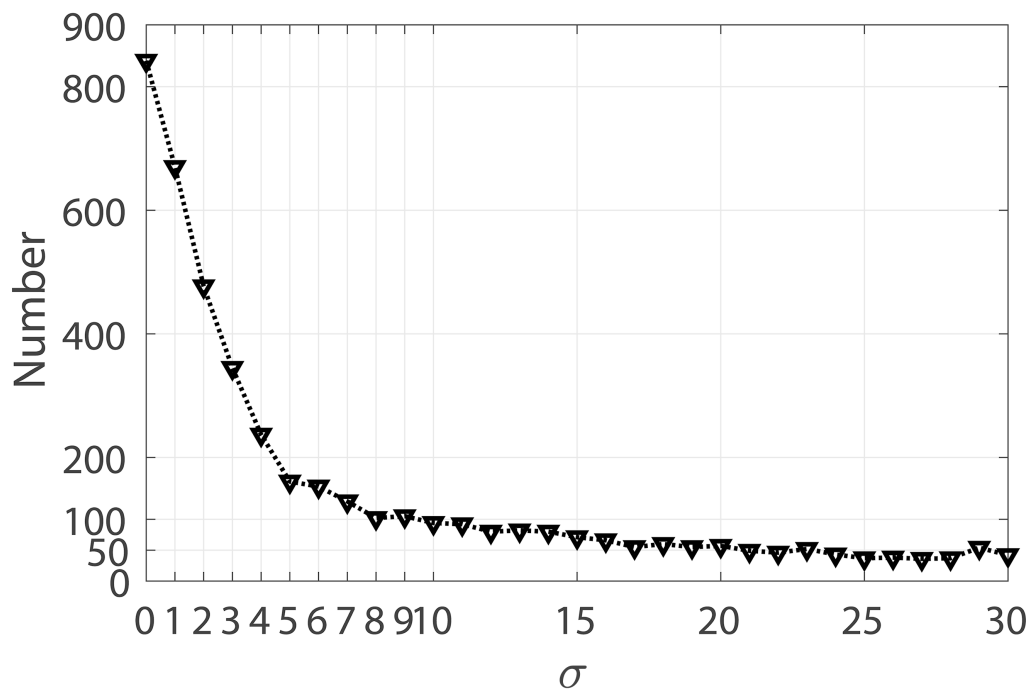


Figure 13: Number of matched PSs as a function of the standard deviation of the disturbance added to the position of the simulated scatterers. The rapid decrease of matched pairs supports the assumption that the vast majority of matches is correct.

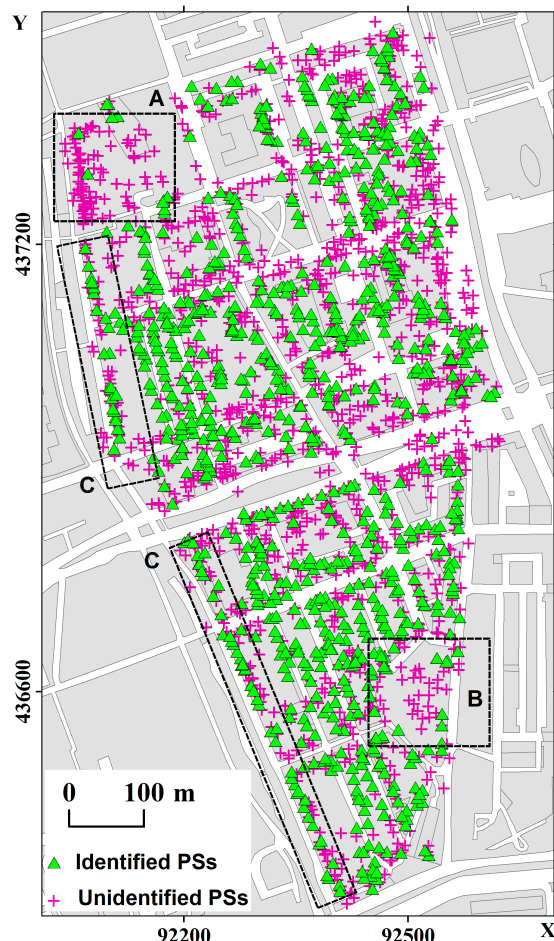


Figure 14: Marched and unmatched PSs. The A-labeled area corresponds to a new building absent in the LOD2 model. The B-labeled area corresponds to a green-area free of buildings, where the PSs correspond to urban structures not included in the model. The C-labeled areas are the examples of predicted PSs at the linear structures of buildings and identified as triple bounce.



Figure 15: Rendering of matched scatterers overlaid on LOD2 city model.

## 4 Conclusion

PS Interferometry can yield deformation with an accuracy of millimeter-order by exploiting PSs. As discussed in the introduction, two key issues in PS Interferometry are the precise geolocation of the scatterers in 3D space, and the association of the scatterers to specific physical features. In this study, we have investigated the use of ray-tracing tools to address the second issue by illuminating 3D city models with different levels of detail (LOD1 and LOD2 according to the CityGML standard). As expected, the results obtained depend strongly on the level of detail of the 3D model given as input to the ray-tracing tool.

For our area of study in Rotterdam we were able to associate 37% of the PSs identified in a stack of TerraSAR-X data with simulated scatterers using a LOD2 city model. Using LOD1 models not only reduced the fraction of identified PSs to around 10%, but also put most of them on the ground. We did not have models for real cities with a higher level of detail. Nevertheless, from the observation of high-resolution SAR data, it is generally understood that many point-like scatterers result from features, such as windows, that are not captured in LOD2. It is expected that using higher LOD models might further increase the fraction of identified scatterers.

Considering the details of the results, it worth noting that roughly one-fourth of the identified PSs were associated to fivefold bounces. These type of scatterers cannot be linked to physical objects by simply intersecting their location with the 3D models.

LOD2 models can be produced automatically from, for example, laser-scanning data. Therefore, it should be expected that LOD2 city models may become commonplace in the near future. The positive results of this study underpin the usefulness of integrating this information in the PS processing.

Associating PSs to physical features is a necessary step if we want to fully exploit the InSAR signal of individual scatterers, for example, to detect deformation of specific sections of a building. In the work presented we have shown that this association can be made. Each simulated PS can be traced back one or multiple reflections on specific locations of the 3D model. However, with

the tools used, the bookkeeping necessary to trace scatterers back to individual features in the model (specific walls, roofs, floors, etc) is still missing. A logical next step in our research is to implement this bookkeeping, which includes identifying practical approaches to label features and, in particular, visualizing the results.

Another important intermediate objective is to investigate, with the support of simulations, how different deformation sources translate to individual PS deformation signals. For example, in the case of a five-fold bounce scatterer, structural deformation may produce a signal with the opposite sign than for a triple-bounce scatterer. As already indicated, the long term goal of the work presented is to improve the interpretation of deformation signals in complex environments, where the observed deformation signals may have different causes. This relies on the anticipated increased availability of high resolution city models.

## Funding

This work was supported by the National Natural Science Foundation of China under Grant 41571435 and Grant 61331016. (Corresponding author: Mingsheng Liao.)

## Acknowledgment

Thanks to Dr. Stefan Auer from the German Aerospace Center (DLR) for helpful discussion on RaySAR. We appreciate the valuable comments of Dr. Ling Chang, the editors, and three anonymous reviewers. Financial support provided to M. Yang by the China Scholarship Council (CSC) during the study in Delft is acknowledged.

## References

- [1] A. Ferretti, C. Prati, and F. Rocca, “Permanent scatterers in SAR interferometry,” *IEEE Trans. Geosci. Remote Sens.*, vol. 39, no. 1, pp. 8–20, Jan. 2001.
- [2] D. Perissin, Z. Wang, and H. Lin, “Shanghai subway tunnels and highways monitoring through cosmo-skymed persistent scatterers,” *ISPRS J. Photogramm. Remote Sens.*, vol. 73, pp. 58 – 67, 2012.
- [3] X. X. Zhu and M. Shahzad, “Facade reconstruction using multiview spaceborne tomosar point clouds,” *IEEE Trans. Geosci. Remote Sens.*, vol. 52, no. 6, pp. 3541–3552, June 2014.
- [4] S. Montazeri, X. X. Zhu, M. Eineder, and R. Bamler, “Three-dimensional deformation monitoring of urban infrastructure by tomographic sar using multitrack terrasar-x data stacks,” *IEEE Trans. Geosci. Remote Sens.*, vol. 54, no. 12, pp. 6868–6878, 2016.

- [5] L. Chang, R. P. B. J. Dollevoet, and R. F. Hanssen, “Nationwide railway monitoring using satellite sar interferometry,” *IEEE J. Sel. Topics Appl. Earth Observ. Remote Sens.*, vol. 10, no. 2, pp. 596–604, Feb 2017.
- [6] X. Qin, M. Liao, L. Zhang, and M. Yang, “Structural health and stability assessment of high-speed railways via thermal dilation mapping with time-series insar analysis,” *IEEE J. Sel. Topics Appl. Earth Observ. Remote Sens.*, vol. 10, no. 6, pp. 2999–3010, June 2017.
- [7] M. Eineder, C. Minet, P. Steigenberger, X. Cong, and T. Fritz, “Imaging geodesy - toward centimeter-level ranging accuracy with terrasar-x,” *IEEE Trans. Geosci. Remote Sens.*, vol. 49, no. 2, pp. 661–671, 2011.
- [8] S. Gernhardt, S. Auer, and K. Eder, “Persistent scatterers at building facades—evaluation of appearance and localization accuracy,” *ISPRS J. Photogramm. Remote Sens.*, vol. 100, pp. 92–105, 2015.
- [9] P. Dheenathayalan, D. Small, A. Schubert, and R. F. Hanssen, “High-precision positioning of radar scatterers,” *J. Geod.*, pp. 403–422, 2018.
- [10] P. Dheenathayalan, D. Small, and R. F. Hanssen, “3D positioning and target association for medium resolution SAR sensors,” *IEEE Trans. Geosci. Remote Sens.*, p. in press, 2018.
- [11] C. Gisinger, U. Balss, R. Pail, X. X. Zhu, S. Montazeri, S. Gernhardt, and M. Eineder, “Precise three-dimensional stereo localization of corner reflectors and persistent scatterers with terrasar-x,” *IEEE Trans. Geosci. Remote Sens.*, vol. 53, no. 4, pp. 1782–1802, April 2015.
- [12] X. X. Zhu, S. Montazeri, C. Gisinger, R. F. Hanssen, and R. Bamler, “Geodetic sar tomography,” *IEEE Trans. Geosci. Remote Sens.*, vol. 54, no. 1, pp. 18–35, Jan 2016.
- [13] A. Schunert and U. Soergel, “Assignment of persistent scatterers to buildings,” *IEEE Trans. Geosci. Remote Sens.*, vol. 54, no. 6, pp. 3116–3127, 2016.
- [14] G. Franceschetti, M. Migliaccio, D. Riccio, and G. Schirinzi, “Saras: a synthetic aperture radar (sar) raw signal simulator,” *IEEE Trans. Geosci. Remote Sens.*, vol. 30, no. 1, pp. 110–123, 1992.
- [15] G. Franceschetti, M. Migliaccio, and D. Riccio, “On ocean sar raw signal simulation,” *IEEE Trans. Geosci. Remote Sens.*, vol. 36, no. 1, pp. 84–100, 1998.
- [16] G. D. Martino, A. Iodice, D. Poreh, and D. Riccio, “Pol-SARAS: A fully polarimetric sar raw signal simulator for extended soil surfaces,” *IEEE Trans. Geosci. Remote Sens.*, vol. 56, no. 4, pp. 2233–2247, April 2018.
- [17] Y. H. Huang, G. Seguin, and N. Sultan, “Multi-frequency and multi-polarization sar system analysis with simulation software developed at CSA,” in *Proc, IGARSS*, vol. 1, 1997, pp. 536–538.

- [18] D. Andersh, J. Moore, S. Kosanovich, D. Kapp, R. Bhalla, R. Kipp, T. Courtney, A. Nolan, F. German, J. Cook, and J. Hughes, “Xpatch 4: the next generation in high frequency electromagnetic modeling and simulation software,” in *Record of the IEEE 2000 International Radar Conference [Cat. No. 00CH37037]*, May 2000, pp. 844–849.
- [19] G. Margarit, J. J. Mallorqui, J. M. Rius, and J. Sanz-Marcos, “On the usage of grecosar, an orbital polarimetric sar simulator of complex targets, to vessel classification studies,” *IEEE Trans. Geosci. Remote Sens.*, vol. 44, no. 12, pp. 3517–3526, 2006.
- [20] H. Hammer and K. Schulz, “Coherent simulation of sar images,” in *Proc SPIE Image Signal Process. Remote Sens. XV* 7477, 2009, pp. 74771K–1–8.
- [21] T. Balz and U. Stilla, “Hybrid gpu-based single-and double-bounce sar simulation,” *IEEE Trans. Geosci. Remote Sens.*, vol. 47, no. 10, pp. 3519–3529, 2009.
- [22] S. Auer, S. Hinz, and R. Bamler, “Ray-tracing simulation techniques for understanding high-resolution sar images,” *IEEE Trans. Geosci. Remote Sens.*, vol. 48, no. 3, pp. 1445–1456, March 2010.
- [23] M. Hazlett, D. J. Andersh, S. W. Lee, H. Ling, and C. L. Yu, “Xpatch: a high-frequency electromagnetic scattering prediction code using shooting and bouncing rays,” *Proceedings of SPIE - The International Society for Optical Engineering*, vol. 2469, pp. 266–275, 1995.
- [24] M. W. Castelloe and D. C. Munson, “3-d sar imaging via high-resolution spectral estimation methods: experiments with xpatch,” in *Proceedings of International Conference on Image Processing*, vol. 1, Oct 1997, pp. 853–856 vol.1.
- [25] R. Bhalla, L. Lin, and D. Andersh, “A fast algorithm for 3d sar simulation of target and terrain using xpatch,” in *IEEE International Radar Conference, 2005.*, May 2005, pp. 377–382.
- [26] S. Auer, “3d synthetic aperture radar simulation for interpreting complex urban reflection scenarios,” Ph.D. dissertation, Technische Universität München, 2011.
- [27] S. Auer, S. Gernhardt, and R. Bamler, “Ghost persistent scatterers related to multiple signal reflections,” *IEEE Geosci. Remote Sens. Lett.*, vol. 8, no. 5, pp. 919–923, 2011.
- [28] S. Auer and S. Gernhardt, “Linear signatures in urban sar images—partly misinterpreted?” *IEEE Geosci. Remote Sens. Lett.*, vol. 11, no. 10, pp. 1762–1766, 2017.
- [29] F. Biljecki, H. Ledoux, J. Stoter, and J. Zhao, “Formalisation of the level of detail in 3D city modelling,” *Comput. Environ. Urban Syst.*, vol. 48, pp. 1–15, Nov. 2014.
- [30] A. S. Glassner, *An introduction to ray tracing*. Elsevier, 1989.
- [31] General 3dfier tutorial to generate LOD1 models, TuDelft 3D Geoinformation, Mar. 2017. [Online]. Available: <https://github.com/tudelft3d/3dfier/wiki/General-3dfier-tutorial-to-generate-LOD1-models>
- [32] Open Geospatial Consortium, “OGC City Geography Markup Language (CityGML) Encoding Standard 2.0.0,” Tech. Rep., Apr. 2012.

- [33] F. Biljecki, H. Ledoux, and J. Stoter, “An improved LOD specification for 3D building models,” *Comput. Environ. Urban Syst.*, vol. 59, pp. 25–37, 2016.
- [34] F. Biljecki, G. B. M. Heuvelink, H. Ledoux, and J. Stoter, “The effect of acquisition error and level of detail on the accuracy of spatial analyses,” *Cartography Geogr. Info. Sci.*, vol. 45, no. 2, pp. 156–176, 2018.
- [35] D. Svirko, P. Krsek, D. Stepanov, and D. Chetverikov, “The trimmed iterative closest point algorithm,” in *Pattern Recognition, International Conference on(ICPR)*, vol. 03, 08 2002, p. 30545. [Online]. Available: [doi.ieeecomputersociety.org/10.1109/ICPR.2002.1047997](https://doi.ieeecomputersociety.org/10.1109/ICPR.2002.1047997)
- [36] D. Chetverikov, D. Stepanov, and P. Krsek, “Robust euclidean alignment of 3d point sets: the trimmed iterative closest point algorithm,” *Image Vision Comput.*, vol. 23, no. 3, pp. 299 – 309, 2005.
- [37] F. van Leijen, “Persistent scatterer interferometry based on geodetic estimation theory” Ph.D. dissertation, Delft University of Technology, 2014.
- [38] G. Boeing, “Osmnx: New methods for acquiring, constructing, analyzing, and visualizing complex street networks,” *Comput. Environ. Urban Syst.*, vol. 65, pp. 126–139, 2016.